

Article

Impact of Rotor–Airframe Orientation on the Aerodynamic and Aeroacoustic Characteristics of Small Unmanned Aerial Systems

Zhenyu Wang ^{1,*}, Quinten Henricks ¹, Mei Zhuang ¹, Anshuman Pandey ², Mark Sutkowy ², Braxton Harter ², Matthew McCrink ²  and James Gregory ² 

¹ Simulation Innovation and Modeling Center (SIMCenter), The Ohio State University, Columbus, OH 43210, USA

² Department of Mechanical and Aerospace Engineering, Aerospace Research Center, The Ohio State University, Columbus, OH 43235, USA

* Correspondence: wang.8516@osu.edu

Received: 19 June 2019; Accepted: 10 July 2019; Published: 12 July 2019



Abstract: With the rapid increase in the number of multi-rotor small unmanned aerial systems (sUAS) in recent years and a plethora of possible applications, the aerodynamic and aeroacoustic characteristics of these vehicles become very important issues. Due to the limited research on the aerodynamic and aeroacoustic characteristics of sUAS which include an airframe or support arm, this paper presents a comprehensive analysis of the flow and acoustic features with the inclusion of said geometry. The influence of rotor orientation—either mounted above or below the airframe—was comprehensively studied through experimental and computational analyses. Detailed experimental investigations—including particle image velocimetry (PIV), pressure transducer readings, and acoustic measurements—were employed to assess the aerodynamic and acoustic characteristics of a rotor–airframe system used on typical multirotor sUAS. The results from the computational methodology were also compared to those from the experiment to assess accuracy and possible benefits.

Keywords: sUAS; aeroacoustics; aerodynamics; rotor airframe interaction; performance

1. Introduction

Small multirotor Unmanned Aerial Systems (sUAS), often referred to as drones, have vertical takeoff and landing (VTOL) capabilities along with good maneuverability that make them an important asset for many applications. They have received unprecedented attention in the past decade due to their adoption in military usage [1], civil applications [2], and scientific research applications [3,4]. Most studies on multirotor sUAS focus on control and photography functions [5] while little research is related to aerodynamics or aeroacoustics. Although the case, aerodynamics, and aeroacoustics of multirotor sUAS should not be disregarded. Multirotor UAS using rechargeable batteries are predicted to have a maximum endurance between 30 and 40 minutes depending on their disc loading and forward flight speed, placing a precedence on aerodynamic efficiency [6,7]. Data collected by Leishman [8] showed that the small-scale rotors used on these systems have a lowered figure of merit, or the ratio of ideal power required to actual power required, compared to rotors on full-scale helicopters. This finding is due to the lower Reynolds number regime that small-scale rotors operate at, meaning viscous forces are more dominant. In this case, figure of merit is an aerodynamic performance metric that is proportional to endurance. In terms of acoustics, the applications previously mentioned typically put sUAS in close proximity to humans, potentially causing annoyance due to emitted noise. It is shown in [9] that a quadrotor UAS weighing 2.1 Kg can produce an overall sound pressure level A-weighting (OASPLA) between 45 and 65 dBA when 35 to 5 meters away, respectively. According

to a psychoacoustic study [10], these overall SPLs would cause the majority of people to be slightly to moderately annoyed. Similarly, it has been shown that drone noise can cause detrimental effects on various animals, a common occurrence due to agriculture and wildlife imagery tasks carried out by drones [3,11]. Due to the previously discussed topics, aerodynamic and acoustic performances become prominent issues likely to affect the design and usage of UAS. Furthermore, it is critical to accurately predict and understand the flow and acoustic characteristics of these systems in order for a more aerodynamically efficient and quiet design to be created.

While aerodynamic performance metrics such as thrust coefficient and power coefficient are important quantitative metrics, they do not provide information on why some rotor geometries are more aerodynamically efficient. In order to better understand why certain performance values are obtained, a form of flow visualization must be used to view the flow characteristics in the wake. Likewise, observing or calculating surface pressures can be used to provide qualitative insights. Past research using smoke flow visualization shows why low Reynolds number rotors are less efficient [12,13]. From the visualization, it is shown that thick wake sheets are produced from the rotors which wander to the center of the wake, causing possible obstruction of the axial velocity. The root portion of the wake sheet was also convected less into the wake, proving that insufficient inflow is produced by this region of the rotor. The shed tip vortices are large and strong relative to the rotor's size and thrust, suggesting that there is considerable downwash and induced drag occurring at this location. Lastly, the wake produced by the rotor contracts significantly; by using one dimensional momentum theory, it can be shown that this attribute causes a reduction in aerodynamic efficiency [8]. While there has been much research investigating isolated small-scale rotors, not much attention has been put on rotor-airframe interactions. Yoon et al. [14] found that there is little difference in thrust production when rotors are mounted above or below the airframe. It was also found that when the rotors were mounted below, there were significant unsteady variations in pressure on the airframe.

Like aerodynamic performance, the acoustic performance of rotors is also affected by the Reynolds number. Isolated low Reynolds number rotors are dominated by tonal noise in the low to mid frequency range, similar to full-scale rotors [2]. At higher frequencies, it is shown that broadband noise is significant for low Reynolds number rotors [15,16]. A computational study revealed that broadband noise is significant at higher frequencies at locations in and out of the rotor plane [17]. This study also showed that noise due to fluid displacement, also known as thickness noise, contributes no noise to a receiver directly above the rotor plane. It was found that above plane noise is dominated by loading and broadband sources. Conversely, in plane noise was found to be affected by all noise sources—thickness, loading, and quadrupole. This same study showed that noise caused by an airframe placed underneath the rotor is significant and that there is up to an 8 dBA (A-weighted sound pressure level) difference in overall sound pressure level when the location of the receiver in the plane of the rotor was altered. If an airframe was not included in the model, the noise at all in plane locations would be the same. It is also acknowledged that airframe noise seems to affect the mid frequencies, between 400 and 1500 Hz, the most [17]. Furthermore, noise from a cylinder in steady crossflow, which is analogous to a cylindrical airframe in the wake of a rotor, produces peaks in noise typically between 400 and 700 Hz, or at the frequency that the lift coefficient is varying [18]. It was found that receiver locations that experienced the greatest noise were normal to portions of the cylinder that experienced the greatest pressure fluctuations. From a study conducted at NASA [19], it is predicted that an airframe that is used above the rotor will cause more noise than one placed below. This is postulated due to the fact that airframe and rotor pressure fluctuations are greater in this particular orientation, causing more noise due to unsteady loading. However, this study does not present acoustic data in the high frequency range and data is only provided at lower blade pass frequency (BPF) harmonics for a single receiver location. Furthermore, this study does not provide flow field results, which may be insightful for acoustic explanations. While blade element momentum theory (BEMT) can be used coupled with the Ffowcs Williams-Hawkings (FW-H) formulation to accurately predict steady loading noise and thickness noise within 3 dB [20], they fail to account for unsteady loading which can be present due to

rotor–airframe, rotor–vortex, and rotor–turbulence interactions. In order to account for these other sources, higher fidelity computational fluid dynamics (CFD) models should be used.

In this paper, aerodynamic and acoustic results were obtained from both experimental and computational methodologies and are used to investigate the impact of airframe orientation (both above and below the rotor) on a multirotor sUAS. Acoustic performance was measured by recording the acoustic spectrum in the far field during anechoic chamber testing. A particle image velocimetry (PIV) technique was used to obtain velocity and vorticity fields while pressure transducers on the cylindrical airframe recorded how pressure changed as the rotor moved azimuthally. Velocity and vorticity fields, pressure, and acoustic results were also simulated by the computational model for comparison purposes. Overall, the focus of this paper is to investigate the impact that airframe orientation has on aerodynamic and acoustic performance. Additionally, this paper will compare and contrast the results from the two methodologies, experimental and computational, to better understand the capabilities of high fidelity simulations and the different experimental strategies employed for this particular application.

2. Physical Model

Instead of using the entire UAS for this study, only a single cylindrical airframe and rotor from the DJI S1000 drone were considered. Figure 1 shows the physical model with the two configurations (i.e., top-mounted and bottom-mounted rotor orientations) employed to investigate the flow and acoustic characteristics. The distance between the rotor and airframe of 27 mm remained constant for the two configurations.

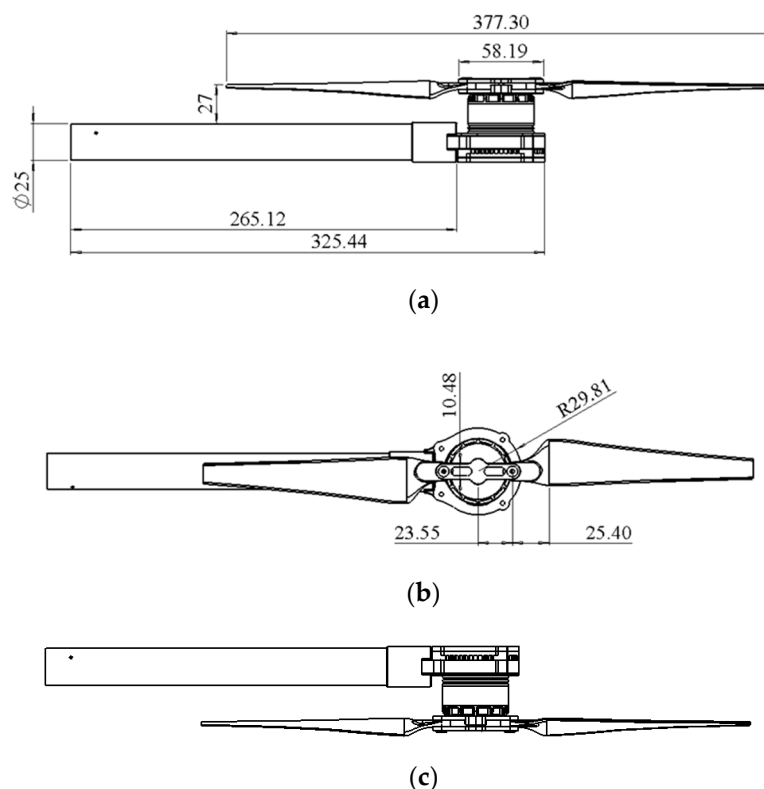


Figure 1. Schematic of rotor (DJI S1000) orientations for (a) top-mounted front view, (b) top-mounted top view, and (c) bottom-mounted front view (dimension: mm).

Additional design information about this particular rotor is given in Figure 2. Figure 2a shows the rotor pitch angle and non-dimensional chord length distributions in the radial direction. It is noticed that approximately linear taper and twist are employed. Specifically, a taper ratio of 0.42 (ratio of

tip chord to root chord) and a linear twist value of -12.5° are used along with a large pitch value of 7.1° at the tip. It can also be seen that a large portion of the rotor (approximately $0.26R$) is cutout due to the motor and connection of the blade. Figure 2b shows the local Reynolds number experienced at different radial locations on the rotor for a rotation rate of 4000 RPM. Based upon [21,22], flow transition of airfoils tends to occur in the Reynolds number range of 50,000 to 70,000 depending on many factors, meaning that the rotor investigated in this study may experience this phenomenon. This is an important Reynolds number regime as laminar separation or laminar separation and reattachment due to transition to turbulent flow can occur, causing degraded performance compared to flows at higher Reynolds numbers. Figure 2c shows the airfoil sections at the root and tip of the rotor blade, which are the same. The airfoil section used is the Althaus AH-6-40-7. This airfoil has a maximum thickness to chord ratio of 6.9% and maximum camber of 5.5% at 40% chord. The particular rotor described in this section is the only geometry tested, both experimentally and computationally. The experimental and computational approaches are described in the following sections.

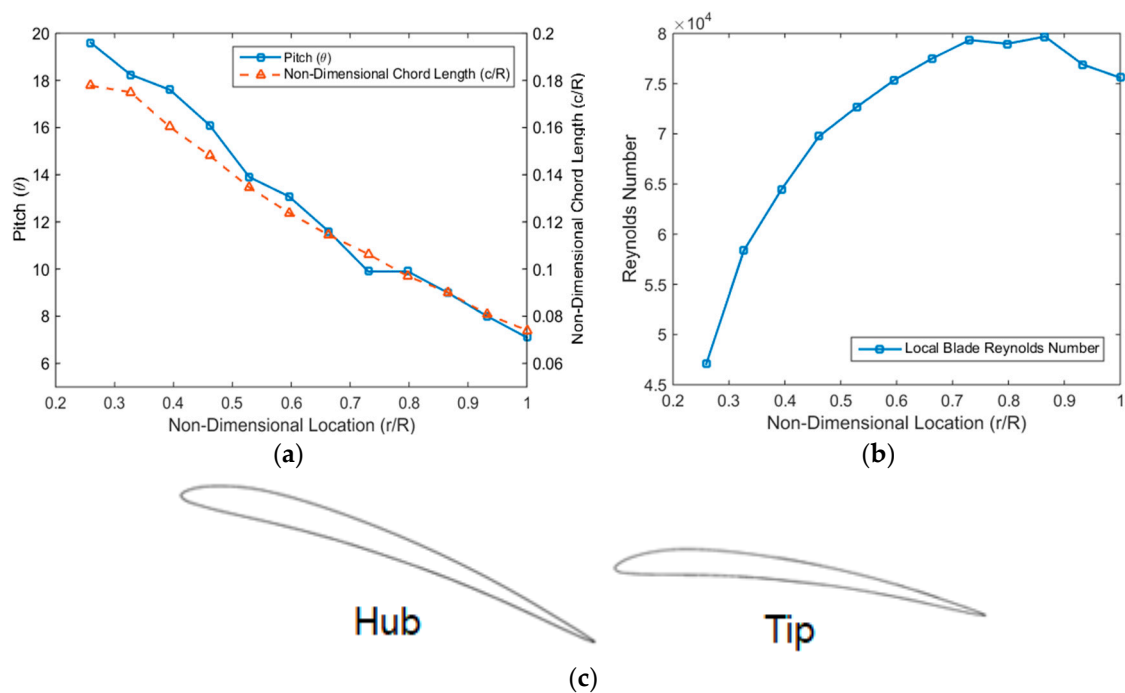


Figure 2. DJI S1000 (a) rotor pitch and chord distribution, (b) local rotor Reynolds number, and (c) root and tip airfoil sections.

3. Experimental Approach

This section describes the methods and measurement techniques used in acquiring flow field characteristics and acoustic data. The rotor geometry described in the previous section was used in two separate configurations to obtain PIV and acoustic data. All experiments used a rotational speed of 4000 RPM.

3.1. PIV Measurement Setup

The PIV setup features a cubical enclosure ($2.0 \times 2.0 \times 1.9$ m) constructed from 80/20 t-slotted extrusion and covered with rigid polypropylene plastic sheeting. The structure houses a test stand upon which the rotor is configured. The two orthogonal sides of the enclosure have been fitted with clear acrylic windows (0.45×0.60 m) to permit laser sheet entry and provide a clear camera field of view. The rotor is mounted in an inverted orientation to a brushless motor such that the wake convects vertically, thus minimizing wake interference from the test stand. An Arduino/LabVIEW interface generates a varying pulse width modulation (PWM) to dictate rotor speed. An optical encoder was

used to track the rotor speed. It features an external red laser mounted directly above and orthogonal to the rotor plane. A phototransistor, mounted directly below the rotor received the encoder laser and was interrupted with each blade passage. The phototransistor generates a digital signal with a frequency corresponding to twice the rotational frequency. A schematic of the system is shown in Figure 3.

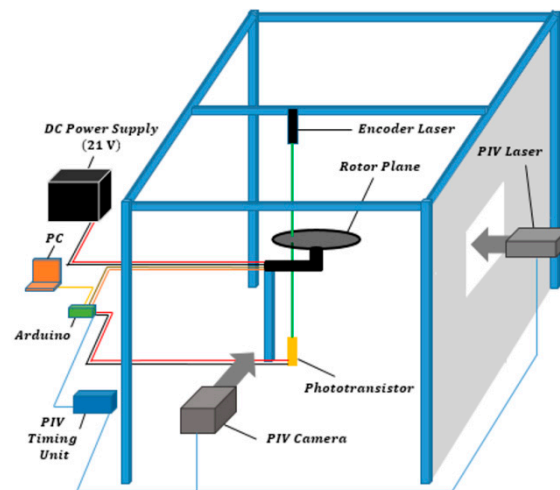


Figure 3. PIV schematic.

Phase-resolved, two-component PIV measurements were made. The PIV configuration included a 16-bit LaVision Imager sCMOS cameras with 35 mm lenses. A New Wave, 532 nm wavelength, Nd: YAG laser generated dual laser pulses. One cylindrical lens was used to generate a laser sheet, and one 1000 mm focal length spherical lens was used to reduce the sheet width to approximately 2 mm at the region of interest. One hundred images were taken at each rotor speed and phase offset combination. This was accomplished by extracting the rotor signal from the optical encoder, generating a designated phase offset using an automated LabVIEW program, and providing the PIV timing unit with the delayed signal. The timing unit was used to synchronize and trigger the PIV cameras and laser. The component orientation and phase increments are illustrated in Figure 4. A time difference of $75 \mu\text{s}$ was found to provide adequate particle correlation with minimal noise. PIV vector calculations were performed using DaVis 8.4.0. Multi-pass, sequential cross-correlation processing parameters were selected. A first-pass window size of 96×96 pixels was used, followed by three passes using a 32×32 pixel window with 50% overlap. More details for the experiments can be found in the paper of Wang et al. [23].

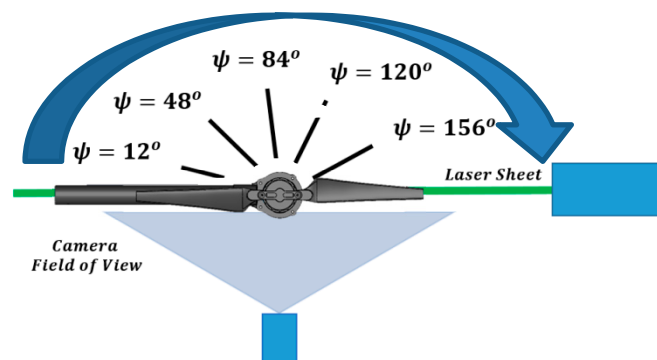


Figure 4. Recorded phase increments.

3.2. Acoustic Experimentation

Acoustic experimentation was conducted in the anechoic chamber at The Ohio State University Aerospace Research Center. Internal dimensions of the facility (wedge-tip to wedge-tip) are $5.14 \times 4.48 \times 2.53$ m tall. Far-field acoustic pressure was acquired in two directions: in the plane of the rotor disc and normal to the rotor disc plane on the inflow side. Both microphones were 1.82 m from the center of the rotor hub. Acoustic testing was completed at a temperature of 16.0 °C and 102.1 kPa atmospheric pressure. The S1000 motor was powered by a 22V DC power supply and the electronic speed control (ESC) signal was provided by an Arduino UNO microcontroller analog pulse width modulation (PWM) output. Rotor frequency was monitored and modulated using a Melexis US5881 Unipolar Hall-effect switch in a feedback loop to the Arduino. The experimental setup is shown in Figure 5.

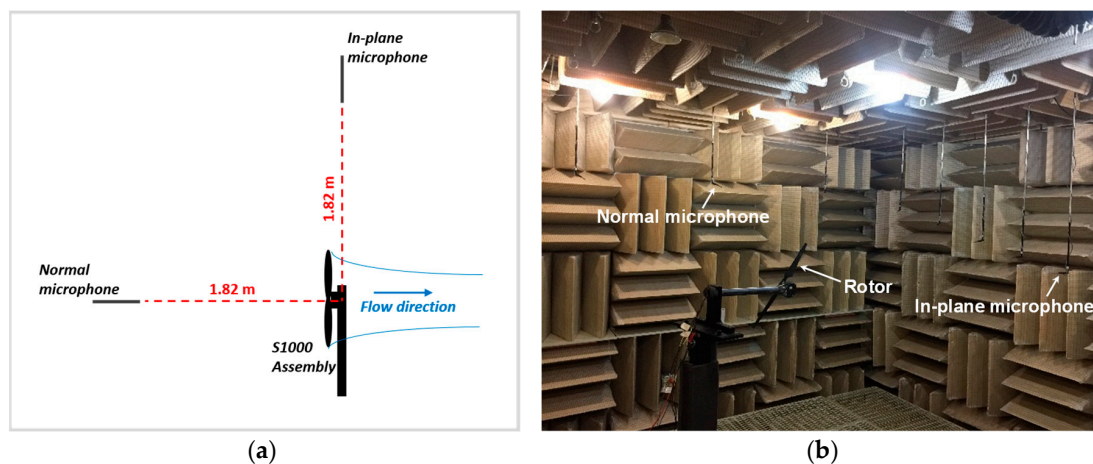


Figure 5. Acoustic testing (a) schematic, and (b) anechoic chamber with rotor assembly and microphones

Acoustic far-field measurements were acquired using two Bruel & Kjaer 4939-A-011 microphones. The signal from each microphone was band-pass filtered from 20 Hz to 25 kHz using a Bruel & Kjaer Nexus 2690 signal conditioning amplifier, and recorded using a National Instruments PXI-6133 A/D board and LabVIEW software. Voltage signals were collected at 50 kHz with 65536 data points per block, resulting in a frequency resolution of 0.763 Hz. 200 blocks were recorded for each case resulting in roughly 60 s of data, allowing for satisfactory convergence of statistics. Data was processed by using a discrete Fourier transform (DFT) with a fast Fourier transform (FFT) algorithm. The pressure power spectrum was converted into sound pressure level (SPL) with units of decibels (dB) using Equation (1), where $P_0 = 20 \mu Pa$ and P is the recorded acoustic pressure.

$$SPL = 20 \log_{10} \frac{P}{P_0} \quad (1)$$

A-weighting was applied in the post-processing of the acoustic data. It should be noted that background (quiescent) noise amplitudes were acquired, but were not subtracted from the data.

4. Numerical Approach

A systematic 3-D numerical simulation was performed in STAR-CCM+ to obtain detailed flow fields including velocity, vorticity, and pressure distributions along with acoustic spectrum results. The computational domain has the same dimensions used for taking PIV measurements. In order to match the boundary conditions used during experimental PIV testing, the boundaries in the simulations were set to be non-slip walls. A pressure outlet condition was used for all boundaries in the acoustic simulations as this strategy mimicked an anechoic environment. A steady Reynolds-averaged Navier–Stokes (RANS) simulation was utilized to yield a fully developed initial flow field for the latter

unsteady simulations. The SST (Menter) k - ω improved delayed detached eddy simulation (IDDES) turbulence model, which combines the features of traditional RANS modeling in the boundary layers and large eddy simulation (LES) modeling in the regions beyond boundary layers, was used in this study [24,25]. In the IDDES model, the dissipation term, ω , in the transport equation for turbulent kinetic energy is substituted for $\tilde{\omega}$ defined as [25]

$$\tilde{\omega} = \frac{\sqrt{k}}{l_{HYBRID}\beta^*f_{\beta^*}} \quad (2)$$

where β^* is a k - ω model coefficient and f_{β^*} is the free-shear modification factor. l_{HYBRID} is the hybrid length scale and is defined as

$$l_{HYBRID} = \tilde{f}_d(1 + f_e)l_t + (1 - \tilde{f}_d)C_{DES}\Delta_{IDDES} \quad (3)$$

where f_e is the blending function; l_t is the turbulent length scale; \tilde{f}_d is a modified version of the equation for f_d ; C_{DES} is a model coefficient; Δ_{IDDES} is the mesh length scale which is dependent on the resolution of the cells in the computational domain. This particular turbulence model was used due to the fact that it is a higher fidelity approach compared to the RANS method. Furthermore, with the turbulent structures being modeled more accurately, the accuracy of acoustic results is improved since much of the unsteady loading and noise is caused by turbulent flow structures. It is further acknowledged that a RANS/LES hybrid approach mitigates the problem of artificially large eddy viscosity, a potential issue of the RANS only model. This issue can lead to inaccurate modeling of vortical structures and boundary layers on or in close proximity to the rotor [14].

In order to mimic rotor motion, the computational domain was split into a rotating region, which encapsulates the rotor, and a stationary region. During the unsteady simulation, the rotating region moved and a sliding mesh technique was used to update the mesh at the interfaces where the rotating and stationary regions contact. A large time step was used for the first several revolutions and then the time step was gradually decreased to achieve better convergence and more accurate results. The final time step employed in the unsteady simulation equals to a 1° azimuthal increment of the rotor blade. A mesh sensitivity study was also conducted to examine if the employed mesh is sufficient to resolve the dominant flow features and to ensure mesh independence. A mesh with 15.3 million trimmed (hexahedral) cells was used in the current study. The meshes near the rotor and airframe were refined accordingly to achieve high-resolution in these regions. Consequently, the wall y^+ values on the rotor blade surfaces and airframe were found to be 1 or less. The mesh was also refined in the wake to resolve convecting flow structures more accurately. Figure 6 illustrates the mesh generated around the rotor, and in the wake region for the top-mounted configuration.

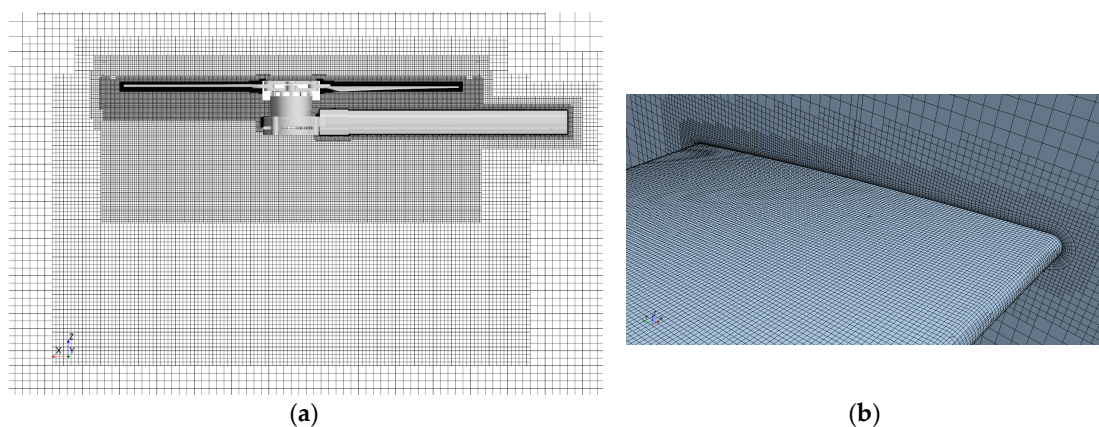


Figure 6. Mesh for the (a) rotor wake, and (b) rotor blade and prism layer.

When a stable unsteady result was attained, the Ffowcs Williams-Hawkings (FW-H) formulation was employed to calculate the far-field acoustic pressure based on the near-field sources, such as the rotor and airframe. The FW-H method is widely known as an effective methodology to predict the sound generated from rigid bodies in arbitrary motion and can be derived directly by reformatting the Navier–Stokes equations into the form of the acoustic wave equation [26]. The thickness and loading terms of the FW-H formulation were considered while the quadrupole term was omitted due to the need for extremely high mesh resolution to calculate this particular source accurately. As discussed in the introduction, this source, which calculates some of the broadband noise, is typically calculated using other means. The thickness term includes noise caused by displaced fluid as the rotor rotates while the loading term calculates noise caused by the pressure distribution on the rotor and airframe. The loading term includes noise caused by both steady and unsteady loading. The thickness and loading terms are represented by monopole and dipole sources, respectively, and are defined by Equations (4) and (5) [27]. This specific mathematical representation of the two sources is called Farassat's 1A formulation.

$$p'_{T}(\mathbf{X}, t) = \frac{1}{4\pi} \left[\int_{f=0} \left[\frac{\rho_0(\dot{U}_n - U_n)}{r(1 - M_r)^2} \right] dS + \int_{f=0} \left[\frac{\rho_0 U_n [r\dot{M}_r + a_0(M_r - M^2)]}{r^2(1 - M_r)^3} \right] dS \right] \quad (4)$$

$$p'_{L}(\mathbf{X}, t) = \frac{1}{4\pi} \left[\frac{1}{a_0} \int_{f=0} \left[\frac{\dot{L}_r}{r(1 - M_r)^2} \right] dS + \int_{f=0} \left[\frac{(L_r - L_M)}{r^2(1 - M_r)^2} \right] dS + \frac{1}{a_0} \int_{f=0} \left[\frac{L_r [r\dot{M}_r + a_0(M_r - M^2)]}{r^2(1 - M_r)^3} \right] dS \right] \quad (5)$$

In Equations (4) and (5), $p'_{T}(\mathbf{X}, t)$ and $p'_{L}(\mathbf{X}, t)$ are the acoustic pressure fluctuations from the mean for the thickness and loading terms, respectively. ρ_0 is the density of the fluid; r is the distance between the source and the receiver; M_r is the Mach number of the source in the direction of the receiver; U_n is the normal velocity of the source surface; M is the Mach number vector of the source; dS is an element of the rotor blade surface; a_0 is the fluid's speed of sound; L_r is the local force that acts on the fluid in the direction towards the receiver; L_M is the local force that acts on the fluid in the direction towards the local Mach number vector of the source. It should be noted that the subscripted quantities in these equations are the inner products of a vector and a unit vector. A variable with a dot above it signifies a time derivative.

5. Results and Discussion

5.1. Vorticity and Velocity Fields

As mentioned above, two rotor configurations (top-mounted and bottom-mounted) were investigated by PIV measurements and numerical studies. Figure 7 illustrates the in-plane vorticity distributions in the PIV measuring plane (i.e., $y = 0$) of the top-mounted case at the phase angle of 156° while Figure 8 shows the bottom-mounted case. The vorticity in the vertical measurement plane (ω_y), which is used to quantify the unsteady turbulent flow characteristics—such as the shedding, breakdown, and dissipating—is defined as

$$\omega_y = \frac{\partial w}{\partial x} - \frac{\partial u}{\partial z} \quad (6)$$

The images shown on the right side of Figures 7 and 8 were obtained from PIV measurement, while those on the left side were extracted from the simulation. The PIV results were averaged by 100 frames at the same phase angle to extract the dominant trends in the flow field. The numerical results were obtained at the specific phase angle when the simulation achieved a statistically stable condition. It can be seen that the simulation results closely resemble the experimental in terms of the shape and magnitude of the flow structures. The vortices shedding from the blade tip (tip vortices) are stronger than those shedding from blade trailing edge (wake sheets). In addition, both the experimental

and simulation results show that the vortices shedding from the blade tip and trailing edge rotate in an inverse direction. The wake sheets are relatively flat, suggesting that uniform inflow and blade loading is achieved; these are qualities obtained by rotors with negative twist and taper. Since this is a two-bladed rotor, each subsequent vortex shown in the wake is 180° older than the previous. As the vortices convect farther axially in the wake, their appearance becomes progressively more smeared. This is a manifestation of tip vortex aperiodicity, a well-known characteristic of these structures.

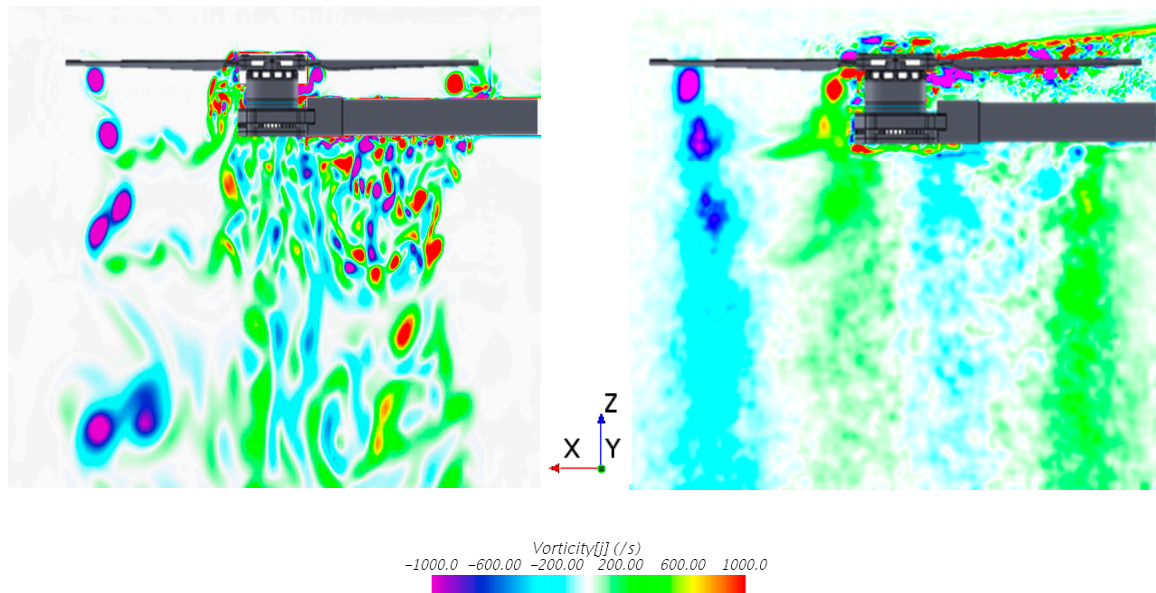


Figure 7. Phase averaged vorticity distribution for top-mounted rotor configuration from simulation (left) and experiment (right).

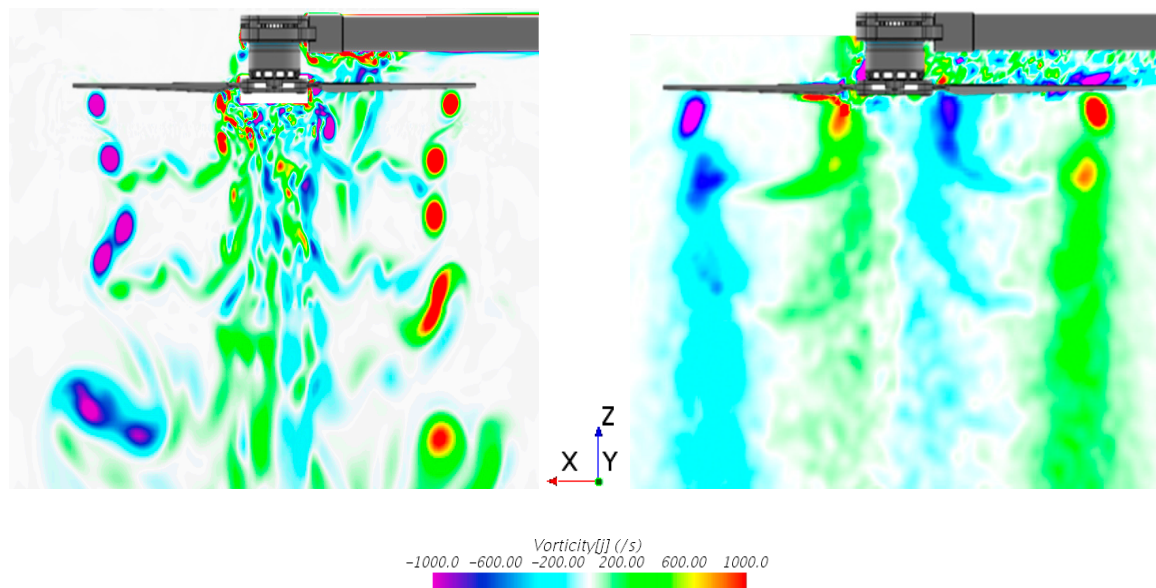


Figure 8. Phase averaged vorticity distribution for bottom-mounted rotor configuration from simulation (left) and experiment (right).

When comparing the vorticity plots from the two separate configurations, there are a couple of distinct differences. For the top-mounted configuration, the rotor experiences fairly clean inflow without any vortical structures. Conversely, the impinging flow on the airframe tends to reflect upwards causing distorted upflow, also known as fountain flow, to interact with the rotor. This observation is noticed more from the experimental findings than the simulation. Additionally, due to the existence of

the below airframe, the convected wake sheets and tip vortices are found to quickly break up into smaller structures. For the bottom-mounted configuration, the rotor experiences distorted inflow with many vortical structures impinging on the rotor blades. Although the case, this inflow condition has very little impact on the convected wake structures. A key difference between the top and bottom mounted rotors is the persistence of the vertical wake structures near the arm for the bottom mounted rotor. These structures do not experience the same impingement and dissipation noted for the top mounted rotor configuration.

Figure 9 shows the time-averaged vertical velocity field in the measurement plane for the top-mounted rotor configuration. The PIV and simulation results indicate a maximum vertical velocity of approximately 12 m/s. In this configuration, it is evident that the flow experiences significant interference from the airframe and an asymmetric shape can be seen in the downstream region because half of the wake is blocked by the airframe. In the undisturbed portion of the wake, the results from the simulation agree very well with those from the PIV measurement. Slight differences occur in the wake region underneath the airframe as the experiment shows the flow accelerating more slowly. Airframe interference and the delay in wake acceleration on this side causes the maximum velocity to be achieved beyond approximately 1.5 times the rotor radius. Overall, the vertical velocity is uniform in the wake, showing an absence of overloading at the rotor tip. This observation agrees with that of the flat wake sheets in Figures 7 and 8, proving that uniform inflow velocity and rotor loading is achieved. Furthermore, the experiment shows that the two separate parts of the wake—unobstructed and airframe obstructed—combine into one large wake while the simulation does not show this finding.

Figure 10 shows the time-averaged vertical velocity field in the measurement plane for the bottom-mounted rotor configuration. Similar to the top-mounted configuration (Figure 9), the simulation results closely match those produced by the experiment. As expected, the wake shape and velocity on the undisturbed side in these two configurations are quite similar. However, both the simulation and experimental results in the bottom mounted case indicate that without interference from the support airframe, the wake velocity is nearly symmetric about the center which illustrates a significant difference in comparison to the top-mounted case. The velocity magnitude from the experiment on the right-hand side of the wake appears to be slightly higher. This could potentially be the result of the support airframe helping speed the flow over the rotor which, in this case, is positioned directly in the rotor inflow. With this configuration, the two separate parts of the wake do not combine into one larger wake, an opposite observation from the top-mounted rotor case.

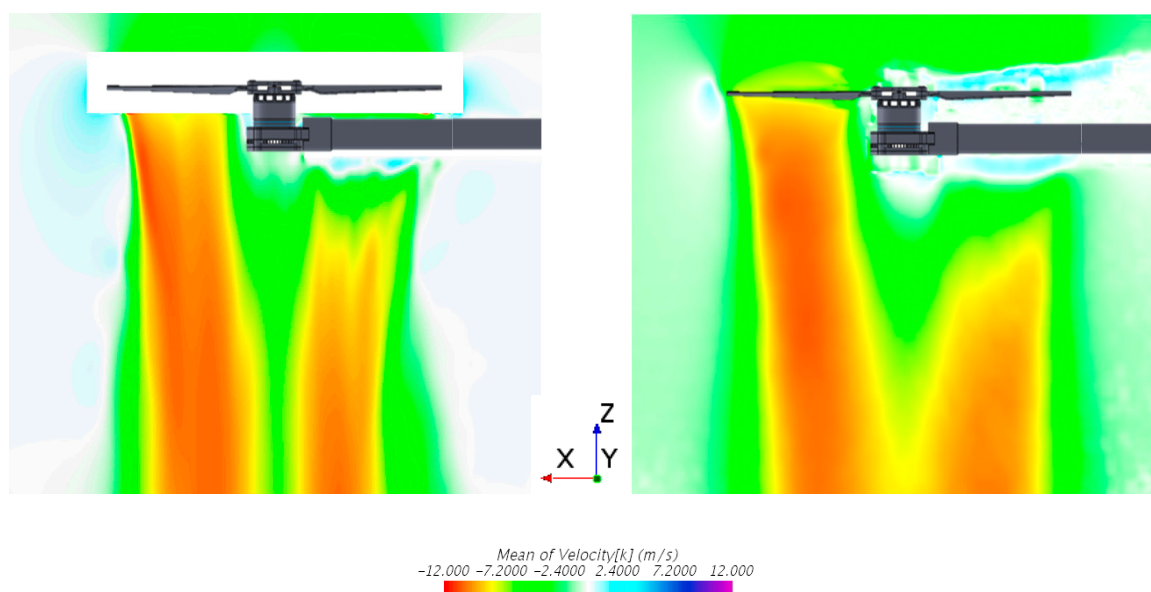


Figure 9. Time-averaged axial flow velocity for the top-mounted rotor configuration from simulation (left) and experiment (right).

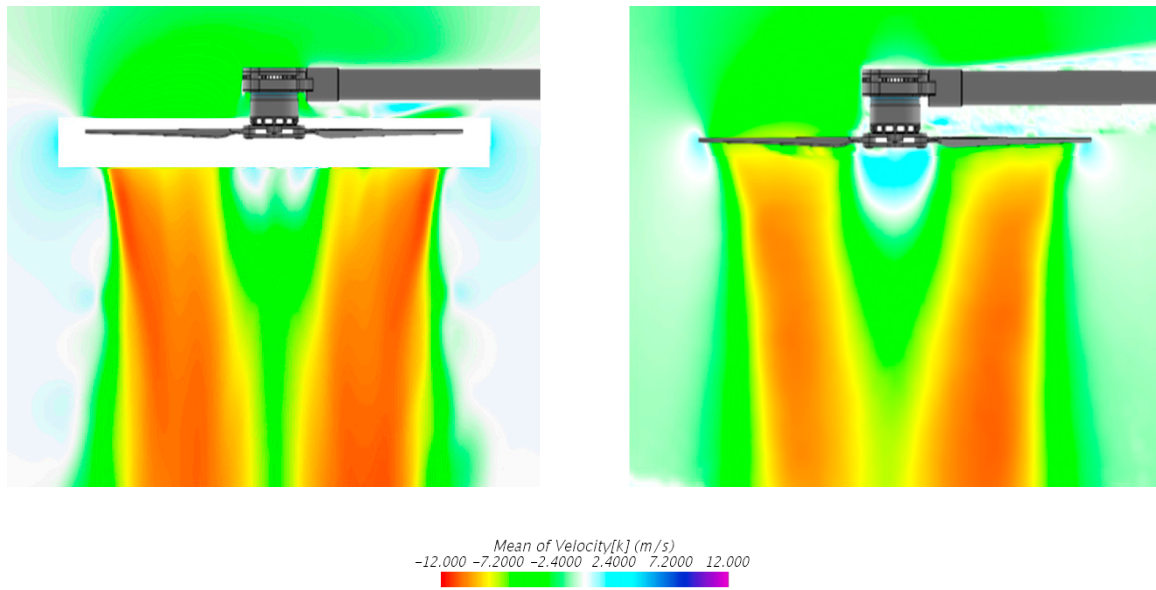


Figure 10. Time-averaged axial flow velocity for the bottom-mounted rotor configuration from simulation (**left**) and experiment (**right**).

5.2. Pressure Contours and Pressure Probe Data

Pressure contours from the simulation are shown in Figures 11 and 12 for the rotor surfaces. While the vorticity and axial velocity measurements show that the rotor is experiencing fairly uniform loading, the pressure contours show that the inboard portion of the rotor is not producing significant lift. Near-zero values of pressure occur at the far inboard locations of the rotor for the top and bottom surfaces thus producing near-zero lift. Furthermore, inboard locations on the top surface appear to experience a significant pressure gradient compared to outboard locations, suggesting an increase in flow detachment from the rotor. It is observed from the contours that there is very little difference in the pressure distribution when comparing the two rotor configurations and azimuth locations. Slight improvements in the pressure distribution on the top and bottom of the rotor surface are seen at inboard locations when the blade is directly over or under the airframe. This benefit is slightly greater for the bottom-mounted configuration.

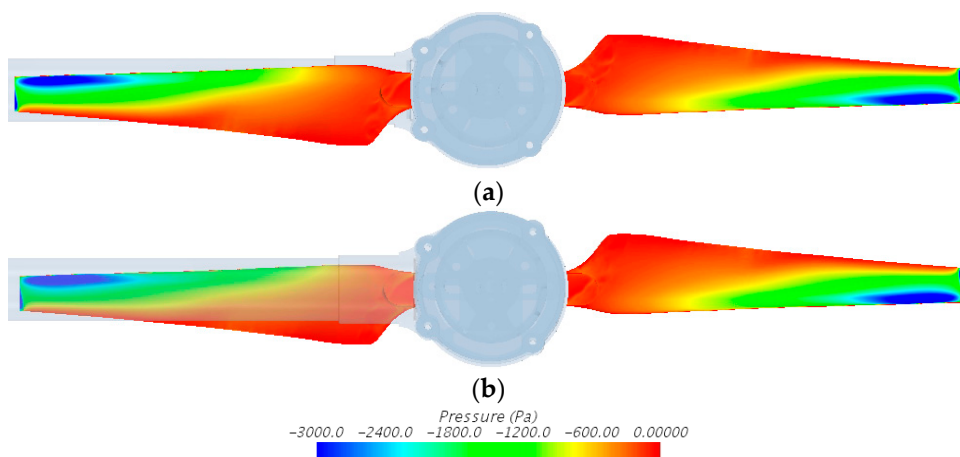


Figure 11. Top rotor surface pressure contours from the simulation for the top-mounted configuration (**a**) and bottom-mounted configuration (**b**).

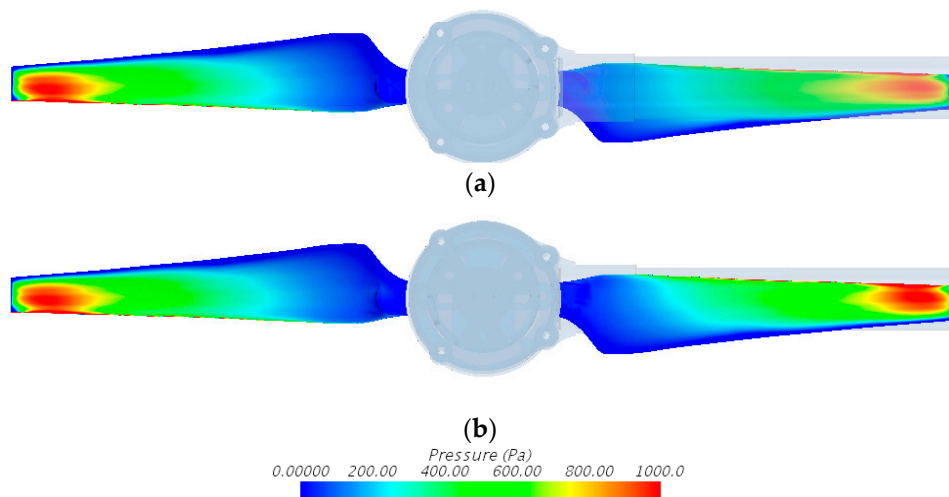


Figure 12. Bottom rotor surface pressure contours from the simulation for the top-mounted configuration (a) and bottom-mounted configuration (b).

Figure 13 shows pressure contour plots for the airframe at azimuth angles that correspond to the rotor's location 24° before being collinear with the airframe ($\Psi = -24^\circ$), collinear with the airframe ($\Psi = 0^\circ$), and 24° past being collinear with the airframe ($\Psi = 24^\circ$). For a two-bladed rotor, an azimuth angle of -24° corresponds to the same blade location as 156° . For the top-mounted case, the pressure is increased from the ambient value on the top location of the airframe while the pressure is decreased on the bottom location as the rotor blade approaches the airframe ($\Psi = -24^\circ$). When the rotor is at an azimuth location of 0° , maximum pressure is observed on the top while the values of pressure on the bottom are further decreased. As the rotor passes at an azimuth location of 24° , the pressure on the top location is reduced and a greater portion of the airframe experiences negative pressure values with greater magnitudes. For the bottom-mounted configuration, the bottom part of the airframe only experiences negative pressures. As the rotor approaches at an azimuth angle of -24° , the airframe's pressure remains unchanged at most locations, but small negative pressures occur on the bottom and back portions of the airframe. When the rotor reaches an azimuth angle of 0° , the bottom portion of the airframe experiences maximum negative magnitudes in pressure with much of the airframe being affected due to the suction surface of the rotor. As the rotor passes at an azimuth angle of 24° , the airframe experiences small negative pressures on the front portion of the airframe. While the airframe in the top-mounted configuration experiences both negative and positive pressures, the bottom-mounted configuration only experiences negative pressures. In both configurations, the airframe experiences similar maximum values in pressure magnitude with a slightly greater area being affected in the bottom-mounted configuration.

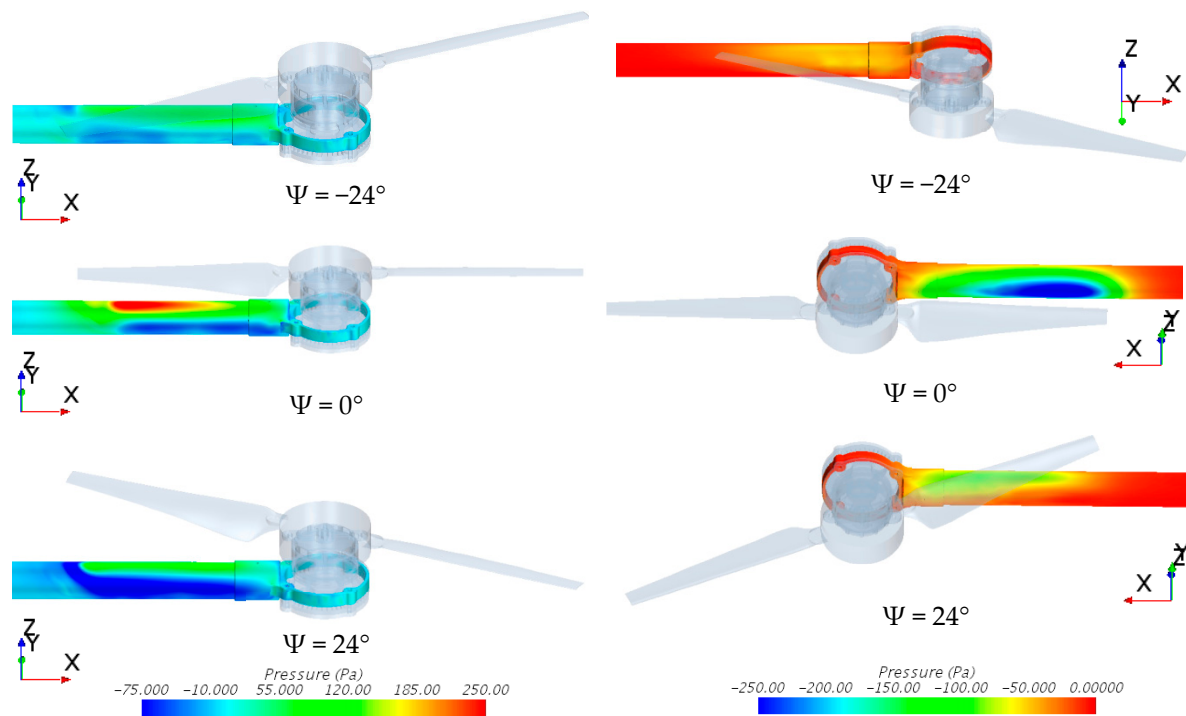


Figure 13. Airframe pressure contours from the simulation for the top-mounted configuration (left) and bottom-mounted configuration (right).

To show how airframe pressure varies over a greater amount of azimuth angles, pressure probe data was also recorded at two separate locations for the two configurations. Figures 14 and 15 show the pressure measured at two probe locations (114 mm and 177 mm) for the separate configurations. The bottom-mounted configuration is shown first in Figure 14 for validation purposes, showing good agreement between the experimental and simulation results. From Figure 15b, it can be seen that pressure spikes occur at both probe locations for the top-mounted configuration. These pressure spikes occur when the rotor is directly collinear with the airframe. Lower values of maximum pressure occur at the outboard probe location due to the fact that the wake contracts significantly, thus the velocity of the flow impinging at this location is lower. The outboard probe also measures negative values of pressure just after the blade passes, an observation that was also noticed from the pressure contours in the top-mounted case in Figure 13. This phenomenon occurs due to the presence of a tip vortex in close proximity to the airframe which causes air to swirl across the airframe surface and up, causing negative pressure. As the vortex impinges on the probe, the pressure increases to near-zero values until the next blade arrives. For the inboard probe, the pressure falls approximately to 45 Pa when the blade is not in close proximity to the airframe. The maximum pressure is around 200 Pa for the inboard probe when the blade is directly over the airframe. The pressure data is less complex for the bottom-mounted configuration since flow and vortex impingement does not occur. For this configuration, maximum negative pressure magnitudes occur when the rotor blade is directly collinear with the airframe. Although the case, this configuration does not produce data that oscillates between negative and positive values and it is seen that pressure values return to near-zero. Pressure values from the two probes are also similar and their maximum magnitudes are greater than that of the top-mounted configuration. Similar pressure values from the two probes occur due to the fact that flow and vortex impingement does not occur in this configuration and also because a rotor with twist and taper makes the pressure distribution on the airframe more uniform [17].

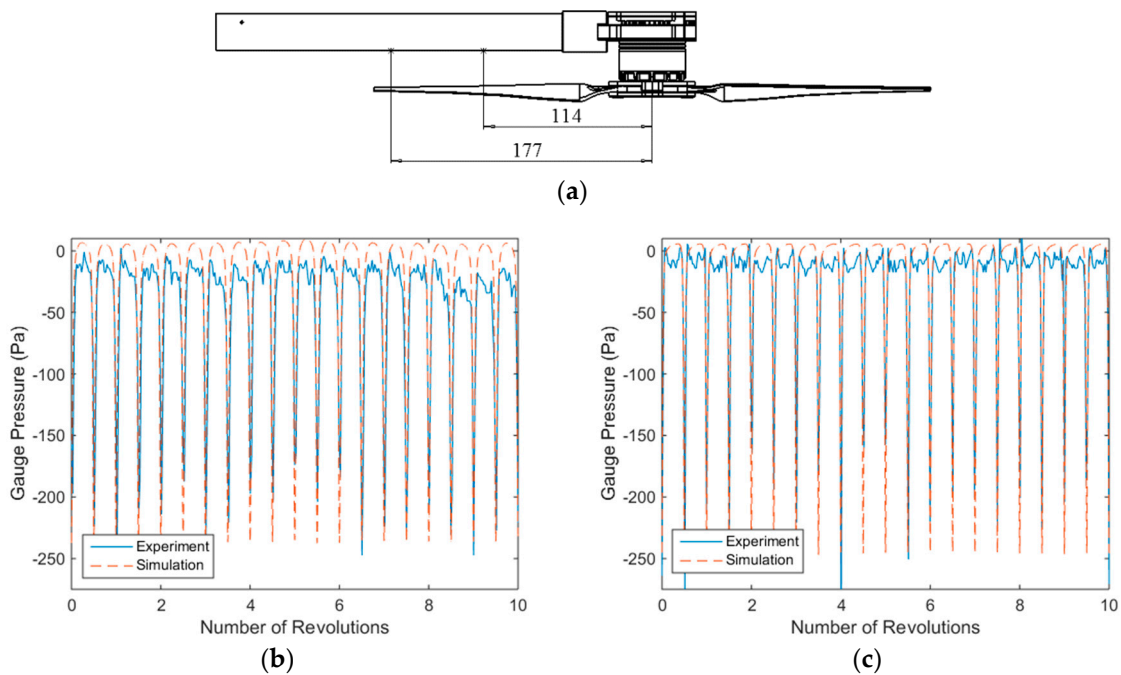


Figure 14. Bottom-mounted configuration (a) pressure transducer locations, (b) pressure from 114 mm transducer, and (c) pressure from 177 mm transducer.

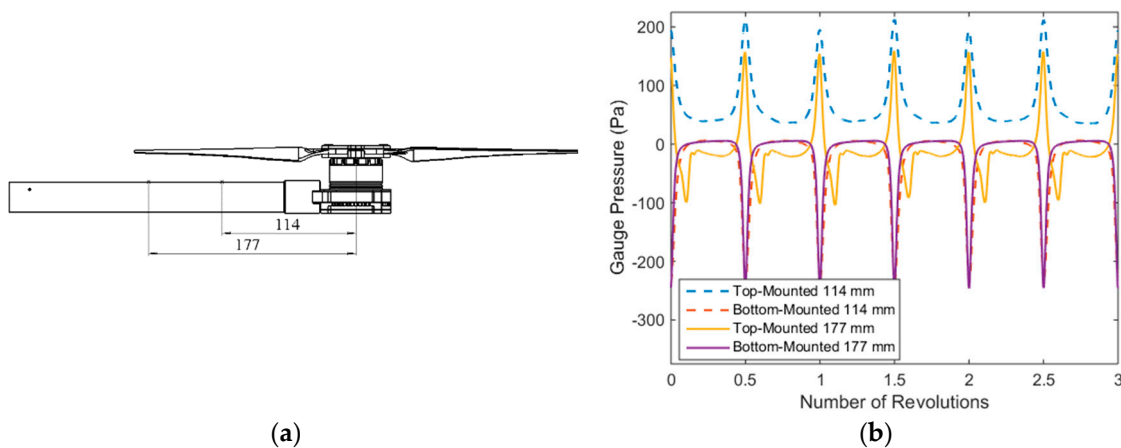


Figure 15. Top-mounted configuration (a) pressure transducer locations, and (b) simulation pressure comparison to the bottom-mounted configuration.

5.3. Acoustic Results

Due to the nature of ESCs, attaining a desired rotational frequency is a challenging task due to the lack of a feedback controller. During acoustic testing, the blade rotational speed was monitored and modulated by using a Hall-effect sensor in a feedback loop with an Arduino microcontroller that provides a control signal to the rotor assembly. This accurately held rotational frequency to the target rotational speed with minimal variance. The variance from the target speed is shown in Table 1.

Table 1. Comparison of target and average rotational frequencies converged upon for acoustic testing.

Target Frequency (RPM)	Target BPF (Hz)	Average BPF (Hz)	Error (%)
4000	133.3	133.5	0.15

Figure 16 shows the sound pressure levels from the in-plane receiver in the frequency domain for both configurations while Figure 17 shows sound pressure levels from the normal receiver. As observed from the results, the BPF and its harmonics are clearly resolved in the experimental data. Both the experimental test and simulation show that broadband noise and tonal noise in the normal direction is notably greater than in the in-plane direction for low to mid frequencies. Additionally, tonal noise is significant compared to the broadband noise up to about 3000 Hz. The simulation is able to accurately predict tonal noise at the BPF and many harmonics of such up to approximately 1500 Hz for both receivers and configurations, but fails to capture broadband noise at the in-plane receiver and at higher frequencies for the normal receiver. This observation is believed to occur due to the contribution of additional noise from the motor/ESC, which is also observed in the study of Intaratep et al. [2]. Another reason for this occurrence is the fact that the simulation did not use a broadband noise model included in the FW-H formulation. As discussed in the introduction, the inclusion of a broadband model is needed to accurately predict higher frequency noise, which is considered to be substantial for low Reynolds number rotors. Thus, for the frequency range beyond 1500 Hz, the experimental data shows greater noise than the simulation. The experimental data also shows the existence of discrete noise spikes which exist between BPF harmonic frequencies. These noise spikes were also observed by Zawodny [15] for an isolated rotor test case and could be caused by mechanical, motor, or noise due to blade asymmetry during the actual operation. It was also found that, at some receiver locations, the airframe was to blame for the existence of tonal spikes between harmonics of the BPF [19]. Although the simulation cannot predict this noise for the in-plane receiver, it appears that it is able to resolve some of these tonal spikes at the normal receiver location, suggesting that the airframe may be radiating this noise. It is also noticed that these tonal spikes between the BPF harmonics are greater in magnitude for the top-mounted configuration. When comparing the two configurations, it is noticed that the bottom-mounted configuration produces greater amplitudes at BPF harmonics and also has greater high frequency noise at the in-plane receiver. At the normal receiver, the bottom-mounted configuration produces more broadband noise in the low to mid frequency range with similar tonal amplitudes being produced in this range for the two configurations. At higher frequencies, the bottom-mounted configuration produces slightly greater broadband and tonal noise.

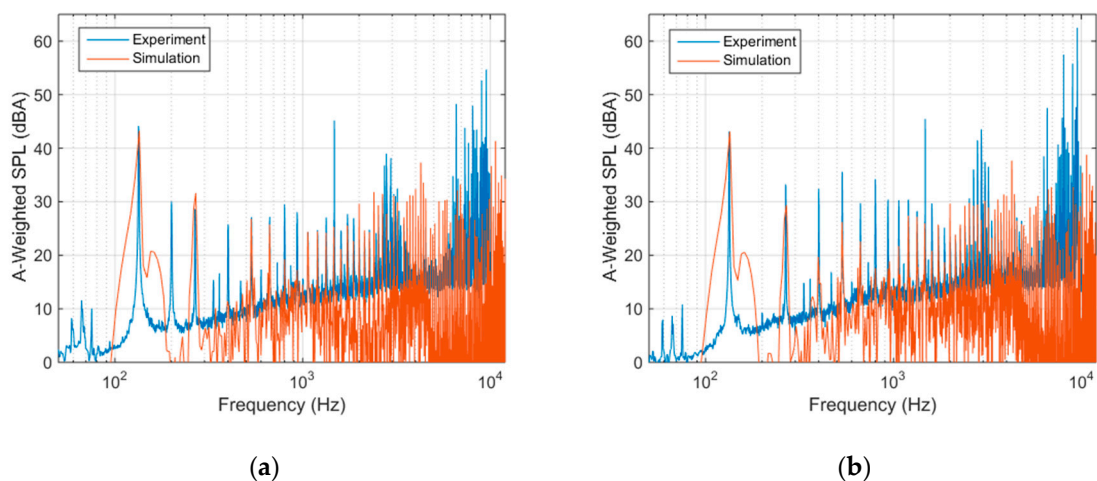


Figure 16. Sound spectra from the in-plane acoustic receiver for the (a) top-mounted, and (b) bottom-mounted configurations.

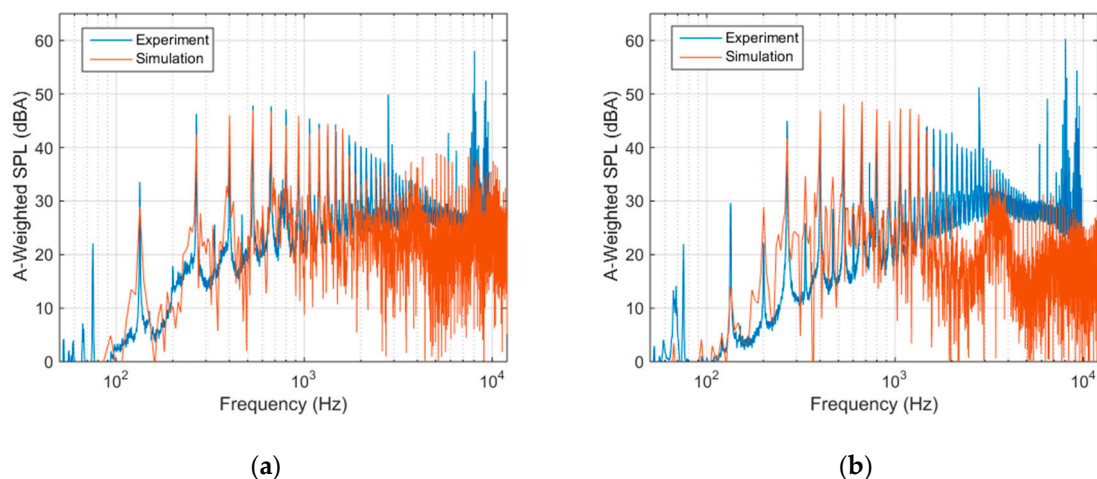


Figure 17. Sound spectra from the normal acoustic receiver for the (a) top-mounted, and (b) bottom-mounted configurations

6. Conclusions

The purpose of this study was to investigate the similarities and differences in aerodynamic and acoustic characteristics for two different configurations (top-mounted and bottom-mounted) of a small UAS/UAV rotor and airframe. A detailed investigation including PIV, pressure, and acoustic measurements, and comprehensive simulations were applied to compare the two configurations.

In summary, it was found that the tip vortices were stronger and rotated in the opposite direction compared to those shed by the trailing edge. Moreover, these vortical structures were well resolved by the simulation, showing similar trends with the experiment such as structure, magnitude, and dissipation as they convected farther axially into the wake. The wake sheets were found to be flat and the axial velocity fields are fairly uniform in magnitude, suggesting uniform aerodynamic loads acting on the rotor blades. It is observed that vortical structures tend to be reflected or generated in the upward direction off of the airframe into the rotor plane for the top-mounted configuration. For the bottom-mounted configuration, vortical structures tend to be sucked into the rotor plane due to the proximity airframe. It is also noted for the top-mounted rotor that the airframe significantly obstructs the flow, causing the magnitude of the velocity to be slower in portions of the wake affected by the airframe.

Pressure contours of the rotor showed that the airframe had little to no impact on the pressure distribution and magnitude on the rotor blades. The contours also implied that little to no thrust is produced by the quarter inner section of the rotor and that the flow detaches on the top portion of the rotor at this location. The pressure contours and measurements from the airframe showed that the top-mounted configuration produced regions of negative and positive pressure while the bottom-mounted configuration only produced negative pressures. Positive pressures occurred for the top-mounted rotor due to flow impingement while negative pressures occurred due to air flowing past the airframe and close proximity tip vortices. The airframe for the bottom-mounted configuration only experienced negative pressures due to the proximity of the suction side of the rotor.

From the acoustic results, it was observed that the bottom-mounted configuration produced more noise at the in-plane receiver due to an increase in the amplitude of BPF harmonics and high frequency noise. For the normal receiver, it was seen that the bottom-mounted configuration produced slightly more broadband noise in the low to mid frequencies. Similarly, this configuration also produced slightly greater tonal and broadband noise in the high frequency range. It can be concluded that these slight increases in noise, which can be seen across the entire spectrum of frequencies, for the bottom-mounted configuration can be attributed to the distorted inflow caused by the airframe. The airframe, in this configuration, not only produces large periodic turbulent structures which can cause tonal noise, but can also cause smaller turbulent structures to continually impact the rotor, resulting in broadband

noise. Overall, the simulation was able to predict tonal noise up to approximately 1500 Hz for both configurations and receiver locations, but was unable to accurately predict broadband and high frequency noise partially due to the lack of a broadband noise model in the FW-H formulation. The lack of accuracy in the high frequency range may also be due to the computational model, which does not consider noise from the motor, mechanical vibrations, ESC, and other sources.

Author Contributions: Conceptualization, Z.W., M.Z., M.M., and J.G.; methodology, Z.W., Q.H., A.P., M.S. and B.H.; software, Z.W. and Q.H.; validation, Z.W., and Q.H.; formal analysis, Z.W. and Q.H.; investigation, A.P., M.S. and B.H.; resources, M.Z. and J.G.; data curation, Z.W. and Q.H.; writing—original draft preparation, Z.W. and Q.H.; writing—review and editing, Z.W. and Q.H.; visualization, Z.W., Q.H. and M.S.; supervision, Z.W., M.Z., M.M. and J.G.; project administration, Z.M. and J.G.; funding acquisition, Z.M. and J.G.

Funding: This work was partially funded by the Ohio State University Simulation Innovation and Modeling Center (SIMCenter) through the support from Honda R&D Americas, Inc.

Acknowledgments: Special thanks to the Ohio Supercomputer Center for providing the computational resources.

Conflicts of Interest: The authors declare no conflict of interest. Additionally, the funders had no role in the research presented in this document or the writing of it.

Nomenclature

c = Rotor chord length (m)
 k = Specific turbulent kinetic energy (m^2/s^2)
 p = Acoustic pressure (Pa)
 P_0 = Reference pressure (Pa)
 M = Mach number (-)
 r = Radial location (m)
 R = Radius of rotor (m)
 t = time (s)
 u = Flow velocity in x direction (m/s)
 v = Flow velocity in y direction (m/s)
 w = Flow velocity in z direction (m/s)
 y^+ = Non-dimensional wall mesh size (-)
 θ = Rotor pitch angle ($^\circ$)
 ψ = Blade phase angle ($^\circ$)
 ω = Specific dissipation rate (1/s)
 ω_y = Vorticity in y -plane (1/s)

References

1. Aleksandrov, D.; Penkov, I. Optimal gap distance between rotors of mini quadrotor helicopter. In Proceedings of the 8th International DAAAM Baltic Conference, Tallinn, Estonia, 19–21 April 2012; pp. 251–255.
2. Intaratap, N.; Alexander, W.N.; Devenport, W.J.; Grace, S.M.; Dropkin, A. Experimental Study of Quadcopter Acoustics and Performance at Static Thrust Conditions. In Proceedings of the 22nd AIAA/CEAS Aeroacoustics Conference, Lyon, France, 30 May–1 June 2016.
3. Lucieer, A.; Turner, D.; King, D.H.; Robinson, S.A. Using an Unmanned Aerial Vehicle (UAV) to capture micro-topography of Antarctic moss beds. *Int. J. Appl. Earth Obs. Geoinf.* **2014**, *27*, 53–62. [CrossRef]
4. Goebel, M.E.; Perryman, W.L.; Hinke, J.T.; Krause, D.J.; Hann, N.A.; Gardner, S.; Leroi, D.J. A small unmanned aerial system for estimating abundance and size of Antarctic predators. *Polar Biol.* **2015**, *38*, 619–630. [CrossRef]
5. Ning, Z.; Hu, H. An Experimental Study on the Aerodynamics and Aeroacoustic Characteristics of Small Propellers. In Proceedings of the 54th AIAA Aerospace Sciences Meeting, San Diego, CA, USA, 4–8 January 2016.
6. Hwang, M.; Cha, H.-R.; Jung, S.Y. Practical Endurance Estimation for Minimizing Energy Consumption of Multirotor Unmanned Aerial Vehicles. *Energies* **2018**, *11*, 2221. [CrossRef]
7. Best Drones with Longest Flight Times. Available online: <https://www.dronethusiast.com/best-drones-with-longest-flight-times/> (accessed on 12 March 2019).

8. Leishman, J.G. *Principles of Helicopter Aerodynamics*; Cambridge University Press: Cambridge, UK, 2006; ISBN 978-0-521-85860-1.
9. Kloet, N.; Watkins, S.; Clothier, R. Acoustic signature measurement of small multi-rotor unmanned aircraft systems. *Int. J. Micro Air Veh.* **2017**, *9*, 3–14. [[CrossRef](#)]
10. Christian, A.W.; Cabell, R. Initial Investigation into the Psychoacoustic Properties of Small Unmanned Aerial System Noise. In Proceedings of the 23rd AIAA/CEAS Aeroacoustics Conference, Denver, CO, USA, 5–9 June 2017.
11. Mulero-Pázmány, M.; Jenni-Eiermann, S.; Strelbel, N.; Sattler, T.; Negro, J.J.; Tablado, Z. Unmanned aircraft systems as a new source of disturbance for wildlife: A systematic review. *PLoS ONE* **2017**, *12*, e0178448. [[CrossRef](#)]
12. Hein, B.R.; Chopra, I. Hover Performance of a Micro Air Vehicle: Rotors at Low Reynolds Number. *J. Am. Helicopter Soc.* **2007**, *52*, 254–262. [[CrossRef](#)]
13. Ramasamy, M.; Johnson, B. Understanding the Aerodynamic Efficiency of a Hovering Micro-Rotor. *J. Am. Helicopter Soc.* **2008**, *53*. [[CrossRef](#)]
14. Yoon, S.; Diaz, P.V.; Boyd, D.D.; Chan, W.M.; Theodore, C.R. Computational Aerodynamic Modeling of Small Quadcopter Vehicles. In Proceedings of the AHS Forum 73, Fort Worth, TX, USA, 9–11 May 2017.
15. Zawodny, N.S.; Boyd, D.D., Jr.; Burley, C.L. Acoustic Characterization and Prediction of Representative, Small-Scale Rotary-Wing Unmanned Aircraft System Components. In Proceedings of the AHS International 72nd Annual Forum, West Palm Beach, FL, USA, 16–19 May 2016; pp. 34–48.
16. Wright, S.E. The acoustic spectrum of axial flow machines. *J. Sound Vib.* **1976**, *45*, 165–223. [[CrossRef](#)]
17. Henricks, Q. A Computational Aerodynamic and Aeroacoustic Study of Small-Scale Rotor Geometries. Bachelor's Thesis, The Ohio State University, Columbus, OH, USA, 2019.
18. Karthik, K.; Vengadesan, S.; Bhattacharyya, S.K. Prediction of flow induced sound generated by cross flow past finite length circular cylinders. *J. Acoust. Soc. Am.* **2018**, *143*, 260–270. [[CrossRef](#)]
19. Zawodny, N.S.; Boyd, D.D., Jr. Investigation of Rotor–airframe Interaction Noise Associated with Small-Scale Rotary-Wing Unmanned Aircraft Systems. In Proceedings of the AHS Forum 73, Fort Worth, TX, USA, 9–11 May 2017.
20. Passe, B.; Baeder, J. Computational Aeroacoustics of Different Propeller Configurations for eVTOL Applications. In Proceedings of the Vertical Flight Society Autonomous VTOL Technical Meeting and Electric VTOL Symposium, Mesa, AZ, USA, 29–31 January 2019.
21. Lissaman, P.B.S. Low-Reynolds-Number Airfoils. *Ann. Rev. Fluid Mech.* **1983**, *15*, 223–239. [[CrossRef](#)]
22. Mueller, T.J. *Aerodynamic Measurements at Low Reynolds Numbers for Fixed Wing Micro-Air Vehicles*; VKI: Sint-Genesius-Rode, Belgium, 1999.
23. Wang, Z.; Pandey, A.; Sutkowy, M.; Harter, B.; McCrink, M.; Gregory, J.; Zhuang, M. A Comprehensive Approach to Study Aerodynamic and Aeroacoustic around Small Multicopter Unmanned Aerial Systems. In Proceedings of the AIAA SciTech Forum, Kissimmee, FL, USA, 8–12 January 2018; Volume 1.
24. Spalart, P.R.; Jou, W.-H.; Strelets, M.; Allmaras, S.R. Comments on the feasibility of LES for wings, and on a hybrid RANS/LES approach. In Proceedings of the First AFOSR International Conference on DNS/LES, Ruston, LA, USA, 4–8 August 1997; pp. 137–147.
25. Shur, M.L.; Spalart, P.R.; Strelets, M.K.; Travin, A.K. A hybrid RANS-LES approach with delayed-DES and wall-modelled LES capabilities. *Int. J. Heat Fluid Flow* **2008**, *29*, 1638–1649. [[CrossRef](#)]
26. Brentner, K.S.; Farassat, F. Analytical Comparison of the Acoustic Analogy and Kirchhoff Formulation for Moving Surfaces. *AIAA J.* **1998**, *36*, 1379–1386. [[CrossRef](#)]
27. Brentner, K.S.; Farassat, F. Modeling aerodynamically generated sound of helicopter rotors. *Prog. Aerosp. Sci.* **2003**, *39*, 83–120. [[CrossRef](#)]

